Metals and Materials International (2019) 25:168–178
https://doi.org/10.1007/s12540-018-0152-1

Influence of Al Addition Upon the Microstructure and Mechanical Property of Dual-Phase 9Cr-ODS Steels

Xiaosheng Zhou[1] · Zongqing Ma[1] · Liming Yu[1] · Yuan Huang[1] · Huijun Li[1] · Yongchang Liu[1]

Received: 25 December 2017 / Accepted: 31 May 2018 / Published online: 12 June 2018

Abstract
With Al addition, dual-phase oxide dispersion strengthened (ODS) steels consisting of martensite and ferrite are fabricated by spark plasma sintering. It is found that Al addition has a negligible effect on martensite lath size, while the amount and size of ferrite grains are related to the Al content. $M_{23}C_6$ (M = Fe, Cr) carbides have been identified within the ferrite grains or along ferrite boundaries. With increasing Al concentration, more fine Y–Al–O oxide nanoparticles are formed. Upon annealing treatment, homogeneous and refined distribution of ferrite grains is obtained, which may involve the particle-stimulated nucleation of recrystallization caused by the large sized $M_{23}C_6$. As Al is increased from 0.05 to 0.1 wt%, the tensile strength of the annealed steel is decreased, as well as its ductility. For the annealed 9Cr-ODS steel containing 0.1 wt% Al, in tensile loading the large sized $M_{23}C_6$ along ferrite boundaries would facilitate the cracking along boundaries between the hard annealed ferrite and soft annealed martensite, producing the mixed fracture of dimple and intergranular fracture.

Keywords Oxide nanoparticle · Al addition · Carbides · Particle-stimulated nucleation

1 Introduction

Oxide dispersion strengthened (ODS) ferritic/martensitic steels have been considered as promising and potential structural materials for both Generation IV fission reactors and advanced fusion reactors, due to their better radiation resistance and high-temperature strength than austenitic stainless steels [1–6]. The excellent performance of ODS steels under hostile service conditions primarily drive from the nanostructured grains and a high density of nanometer-scale oxides with good thermal stability [7, 8]. In terms of matrix structure, the ODS steels can be classified into martensitic/dual-phase martensitic–ferritic steels containing 0.1–0.2 wt% C and 9–11 wt% Cr, and ferritic steels containing 12 wt% Cr or above. The α-γ transformation of 9–11 wt% Cr transformable steels can produce more equiaxed grains and thus reduce the mechanical property anisotropy, facilitating the effective control on structure and processing of these steels [9, 10].

Nevertheless, high-temperature resistance of transformable steels is generally inferior to that of ferritic steels, especially those steels with full martensitic structure [7]. As the pinning force for α/γ boundary by oxides overcomes the driving force for α-γ transformation, certain amount of metastable ferrite is retained, yielding ferrite-martensite dual-phase structure [11]. Japan paid considerable attention to the development of dual-phase transformable steels [12–16]. It was found that creep strength of 9Cr-ODS steels can be significantly improved by the optimum balance between tempered martensite and residual ferrite, and the amount of residual ferrite can be tailored by adjusting the concentrations of Ti and excess O (the value obtained by subtracting oxygen concentration coupled with yttrium in Y_2O_3 from total oxygen concentration in steel) [11, 17, 18].

With respect to nano-particle control in ODS steels, various types of alloying elements were added in small quantities to react with Y_2O_3, forming nano-clusters or complex oxides like Y–Ti–O, Y–Al–O or Y–Zr–O oxides [19–24]. However, the published literature is usually concerned with non-transformable ferritic steels. The effects of alloying elements on microstructure and mechanical performance of 9Cr

✉ Zongqing Ma
mzq0320@163.com

✉ Yongchang Liu
licmtju@163.com

[1] State Key Lab of Hydraulic Engineering Simulation and Safety, School of Materials Science and Engineering, Tianjin University, Tianjin 300354, People's Republic of China

transformable steels are seldom reported. Ohtsuka et al. studied the high-temperature strength of hot-extruded 9Cr-ODS steels with small amount of Al addition (< 0.1wt%). The ultimate tensile strengths at 700 and 800 °C are decreased with increasing Al concentration [25]. Since Al is a ferrite stabilizer, in this work small amount of Al is also added to ensure the ferrite-martensite dual-phase structure. Spark plasma sintering (SPS), one comparatively novel sintering process with fast heating rate and short holding time, will be used to fabricate the 9Cr-ODS bulk. The microstructure of the 9Cr-ODS steels with Al addition will be characterized in detail, and their mechanical property will also be evaluated, to provide important information for nano-mesoscopic structure control in transformable 9Cr-ODS steel.

2 Experimental Procedures

Pre-alloyed powders with the nominal composition Fe-9Cr-0.1C-2 W-0.2 V-0.07Ta (in weight) were produced by inert-gas atomizing, and 0.05 and 0.1 wt% Al element powders were respectively blended with the pre-alloyed powders and 0.35 wt% Y_2O_3 nanoparticles. Then, the mixed powders were mechanically milled in an argon atmosphere in a planetary ball mill for 45 h. The rotation speed was 400 rpm, and the ball-to-powder ratio was 15:1. The mechanically milled powders were capsuled in a graphite die with 20 mm inner diameter, and consolidated by SPS with Dr. Sinter SPS-625 machine. Compacts of about 20 mm diameter and 15 mm height were obtained. The detailed sintering regime was as follows: powders were first heated to 800 °C for 5 min at a rate of ~ 100 K/min, and then continuously heated to 1100 °C for 10 min with an pressure of 40 MPa, followed by continuous cooling in spark plasma furnace. The SPSed steels were annealed at 800 °C for 1 h under Ar protection, aimed at restoring ductility. In this study, the 9Cr-ODS steel containing 0.05 wt% Al and 0.1 wt% Al is respectively referred as 9Cr-0.05Al steel and 9Cr-0.1Al steel.

The microstructures of 9Cr-0.05Al and 9Cr-0.1Al steels in sintered and annealed conditions were examined through optical microscopy (OM), scanning electron microscope (SEM) and high resolution transmission electron microscope (HRTEM). For OM and SEM observation, metallographic specimens were etched in a mixed solution of water (100 mL), hydrochloric acid (20 mL) and iron trichloride (5 g). Standard 3 mm TEM discs were ground to a thickness of about 0.07 mm and then thinned by twin-jet electropolisher with a solution of 5 vol.% perchloric acid in ethanol. To evaluate the hardness of martensite, tempered martensite and ferrite, Vickers microhardness testing was performed with 25 g load and 5 s dwell time. Micro-tensile test was carried out to clarify the effects of Al addition on mechanical properties of annealed steels. The gauge size of plate tensile samples is 5 mm (length) × 1.5 mm (width) × 2 mm (thickness), and prior to tensile test, certain stress was imposed on tensile specimen to make it upright. The fracture surface was examined by SEM.

To quantitatively analyze the volume fraction and size of residual ferrites with different Al contents, the optical micrographs were processed by image processing software to examine the distribution of ferrite in matrix. The area fraction and sizes of ferrite can be obtained in image analysis software. In this work, the area fraction of ferrite is estimated as its volume fraction, and the length of the line joining two points of ferrite outline and passing through the centroid is defined as the ferrite size.

3 Results and Discussion

3.1 SPSed Condition

Figure 1a, d respectively shows the optical micrograph of as-sintered 9Cr-0.05Al steel and 9Cr-0.1Al steel. The dark region represents martensite while the bright region represents ferrite. Ferrite grains are uniformly distributed, and some large-sized aggregates of ferrite grains can also be observed, as indicated by the yellow arrows in Fig. 1a, d. Figure 1b, e is respectively the image obtained by processing Fig. 1a, d with image software, clearly displaying the ferrite distribution. It can be seen that the boundaries of ferrite are not straight but unshaped. The aggregated ferrite grains appear to be compressed, and the size of aggregates can be up to 30–40 μm. The ferrite formation may involve the increase in pinning force for α/γ boundary by the formation of Y–Al–O oxides, or the decrease in driving force for α-γ transformation by Al alloying. Size distribution of ferrite in 9Cr-0.05Al steel and 9Cr-0.1Al steel is respectively presented in Fig. 1c, f. The mean ferrite size of 9Cr-0.05Al steel (5.1 ± 3.3 μm) is slightly smaller than that of 9Cr-0.1Al steel (5.7 ± 4.4 μm), and the larger percent of ferrite with size larger than 15 μm in 9Cr-0.1Al steel should also be noted. The volume fraction of ferrite in 9Cr-0.05Al steel and 9Cr-0.1Al steel is respectively estimated as 18.7 ± 0.5% and 17.1 ± 0.8%. With the increase in amount of Al addition, the volume fraction of ferrite is decreased, which may be related to the non-equilibrium microstructures in mechanically-alloyed alloys [25].

Figure 2 represents the TEM images of 9Cr-0.05Al and 9Cr-0.1Al steels, displaying morphologies of martensite. Martensite laths can be clearly seen in both 9Cr-0.05Al and 9Cr-0.1Al steels, as shown in Fig. 2a, c. However, different from the lath martensite in conventional ferritic/martensitic heat resistant steels, the laths in 9Cr-0.05Al and 9Cr-0.1Al steels exhibit much smaller lengths, meaning smaller aspect ratio values. The width of martensite laths in these

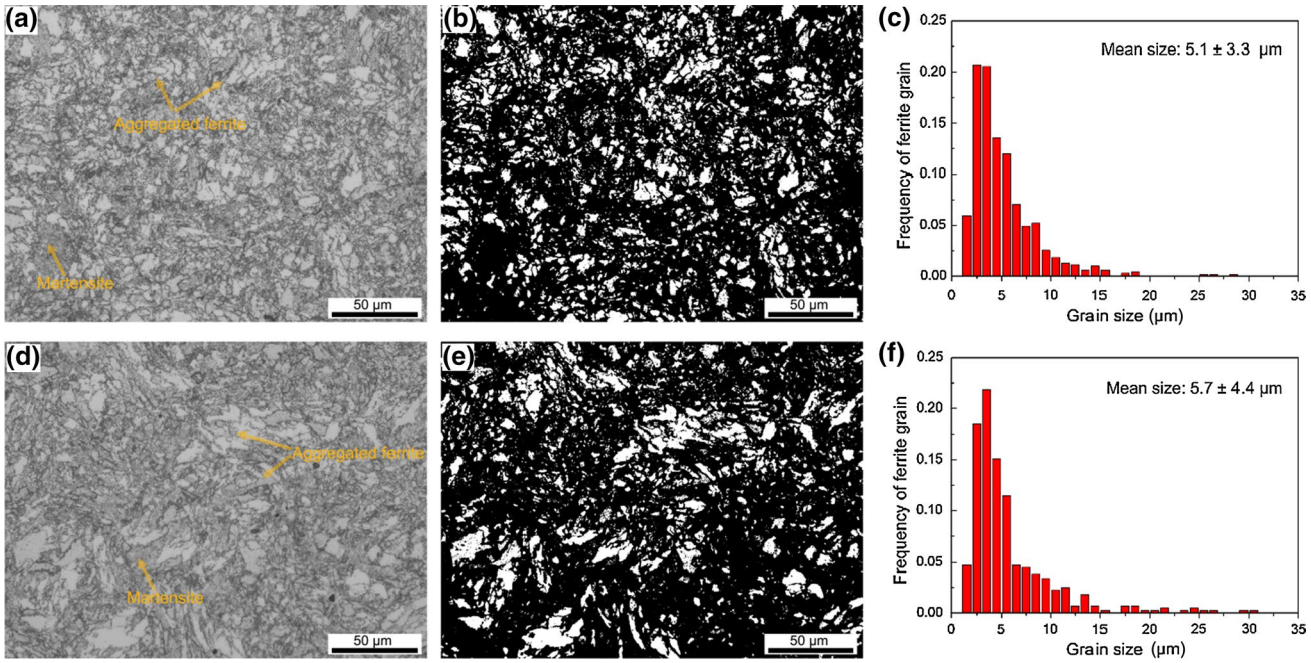

Fig. 1 Optical micrograph, ferrite distribution and the size frequency of ferrite in sintered 9Cr-ODS steels with different Al contents. **a**–**c** 0.05 wt% Al added, and **d**–**f** 0.1 wt% Al added

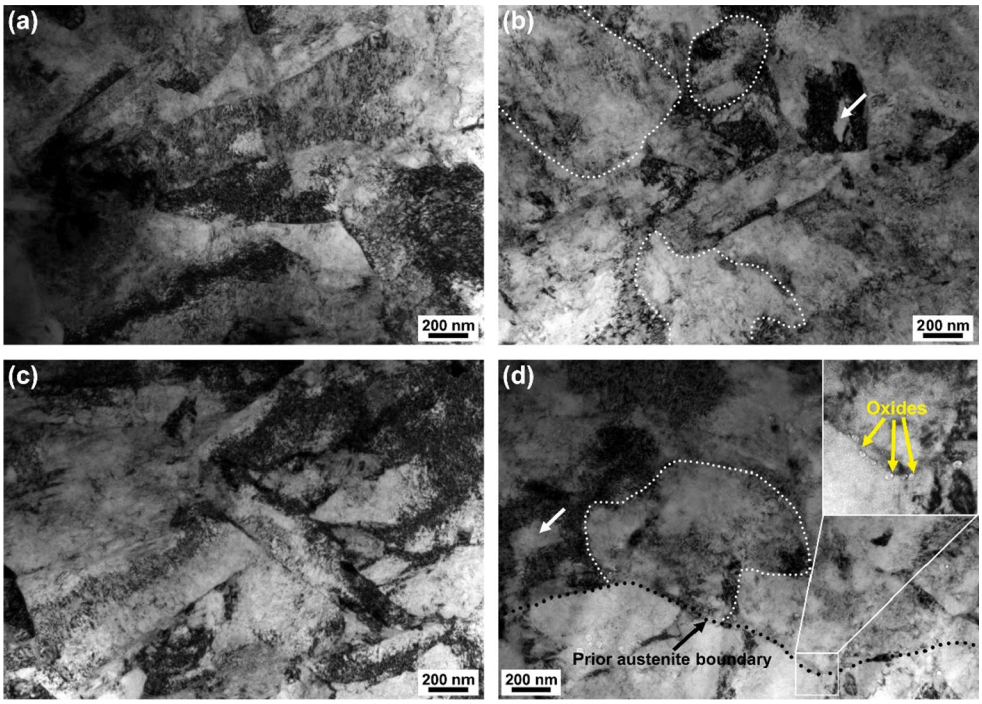

Fig. 2 Martensite exhibiting different morphologies in SPSed **a** and **b** 9Cr-0.05Al and **c** and **d** 9Cr-0.1Al steels

two steels changes from dozens to hundreds nanometer, and Al addition has a negligible effect on the size of lath martensite. High density of dislocations can also be readily seen, and they derive from either martensitic transformation or the dislocations retained due to fast heating rate and short holding time in SPS. The lath characteristics cannot always be observed, as shown in Fig. 2b, d. In Fig. 2b, the short martensite lath is surrounded by the martensite without lath

morphologies, and in Fig. 2d, it seems that martensite is divided by the low-angle boundaries consisting of dislocations. It is suggested that the martensite without lath characteristic is still supersaturated with carbon, and it is related to the annihilation of high density of dislocations. As indicated by the white arrows in Fig. 2b, d, piled dislocations enclose a region with low density of dislocations, which is suspected to represent the product of dislocation annihilation. In Fig. 2d, one prior austenite grain boundary at the bottom of the micrograph appears waved in shape owing to the pinning effect of oxide particles which are marked by yellow arrows.

In TEM examination of SPSed 9Cr-0.05Al steel, long striped microstructure was occasionally found within martensite, as shown in Fig. 3a. Figure 3b, c respectively represents the diffraction pattern of the striped microstructure and the matrix. Based on the diffraction pattern in Fig. 3b, the striped microstructure is identified as iron aluminide (Fe_3Al). The striped microstructure was just observed in SPSed 9Cr-0.05Al steel for once, and in SPSed 9Cr-0.1Al steel, the similar microstructure was not found. Its formation is suggested to be related to the segregation of Al in iron matrix caused by inhomogeneous mechanical milling.

Regarding the ferrite in 9Cr-0.05Al and 9Cr-0.1Al steels, Fig. 4 displays more details. In 9Cr-0.05Al steel, $M_{23}C_6$ (M = Fe, Cr) carbides are precipitated within ferrite grains (Fig. 4a), along martensite/ferrite boundaries and ferrite/ferrite boundaries (Fig. 4b). Long $M_{23}C_6$ carbides are formed at boundaries, while more globular $M_{23}C_6$ precipitates are distributed in ferrite grains. The distribution of $M_{23}C_6$ in ferrite is not homogeneous. Nano-sized oxides can also be found in ferrite grains, as shown in Fig. 4b. As the Al addition is increased to 0.1 wt%, $M_{23}C_6$ carbides with larger size are prone to precipitate, and the density of $M_{23}C_6$ carbides within ferrite grains is decreased. It should also be noted that in some areas, the boundary between ferrite and martensite is not distinct, and the ferrite is transited to martensite, as marked with dotted line in the lower right corner in Fig. 4d. For the transformable ODS steels, the residual ferrite formed in heating stage by pinning effect of oxides on α/γ boundaries represents a ferrite phase that would not be transformed at austenitization temperature. On the other hand, in cooling stage transformed ferrite phase may also be produced by austenite to ferrite transformation, which is related to the austenite stability and cooling rate. Oka et al. [26] suggested that residual ferrite and transformed ferrite can be distinguished in terms of grain size, dislocation density and number density of nano-sized oxides in them. Residual ferrite has smaller grain size, higher dislocation density and larger number density of oxides than transformed ferrite. However, no carbides were found in either residual ferrite or transformed ferrite [26]. Since the size of octahedral interstice in b.c.c. iron is much smaller than that in f.c.c. iron, the solubility of carbon in ferrite is much smaller than that in austenite [27]. For the residual ferrite that can be stable at austenitization temperature, carbon atoms tend to dissolve into austenite, and carbides would not precipitate within residual ferrite. Moreover, in our previous study concerning the SPSed 9Cr-ODS steel without Al addition, small amount of residual ferrite without carbide precipitation has been observed, and the ferrite boundaries are also clean [28]. Here, if the austenite to ferrite transformation occurs upon cooling, the low solubility of carbon in ferrite would facilitate the carbide precipitation. Thus, in this work, ferrite in SPSed 9Cr-0.05Al and 9Cr-0.1Al steels should be the transformed ferrite, rather than the residual ferrite. Since the austenite is not completely transformed into ferrite, the remained austenite transforms to the martensite supersaturated with carbon atoms. The microstructure of SPSed 9Cr-0.05Al and 9Cr-0.1Al steels consists of martensite and transformed ferrite.

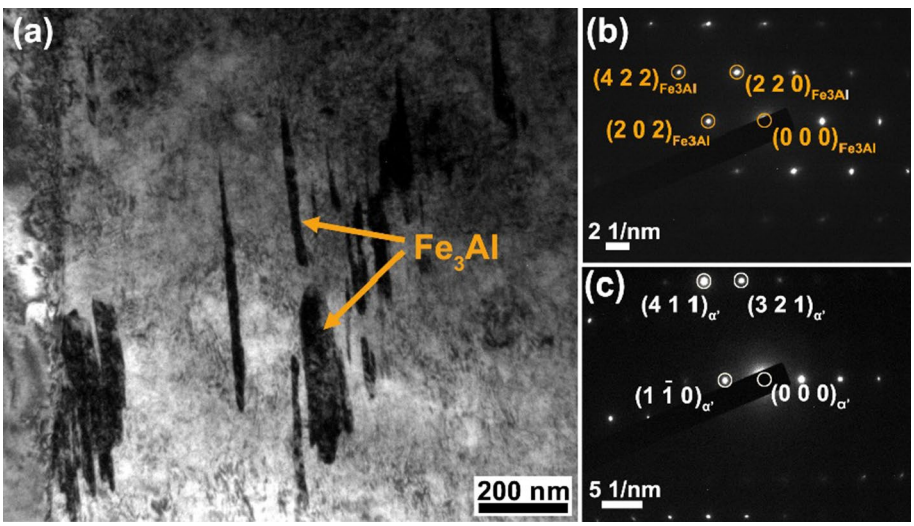

Fig. 3 **a** TEM image of Fe_3Al in SPSed 9Cr-0.05Al steel and the diffraction patterns of, **b** Fe_3Al and the matrix

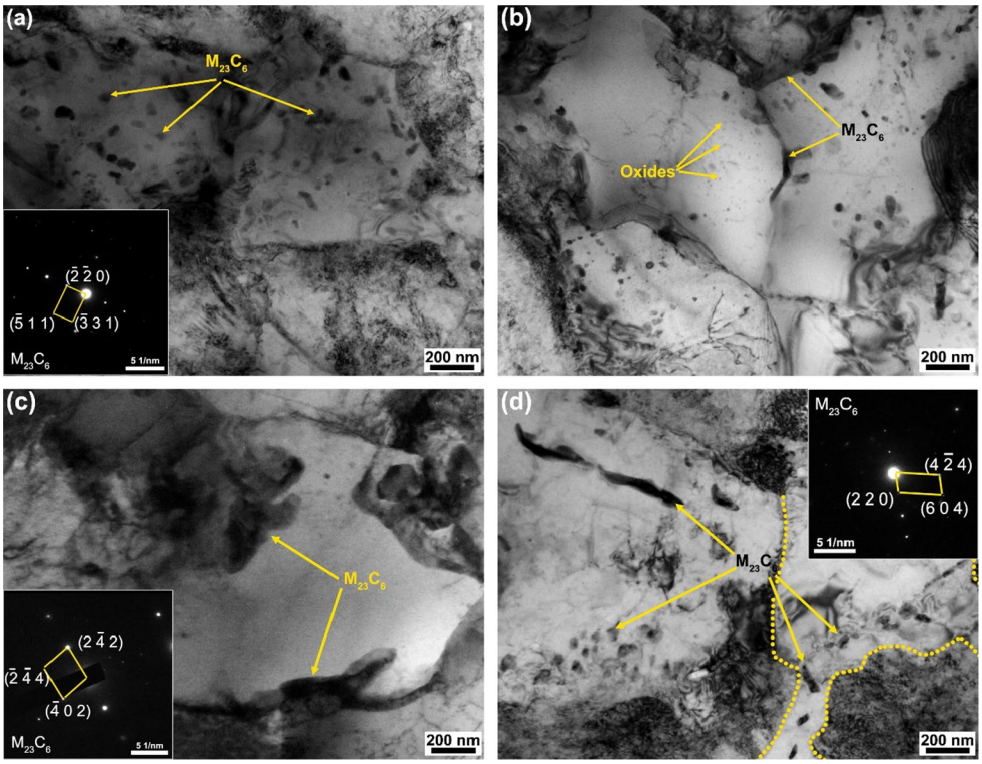

Fig. 4 TEM images showing the ferrite and carbides in SPSed **a** and **b** 9Cr-0.05Al and **c** and **d** 9Cr-0.1Al steels. The insets give the diffraction patterns of carbides

Figure 5 shows the SEM images of 9Cr-0.05Al and 9Cr-0.1Al steels, from which it can be more clearly seen that Al addition has a significant effect on the $M_{23}C_6$ carbides in SPSed 9Cr-0.05Al and 9Cr-0.1Al steels. In the 9Cr-0.05Al steel, $M_{23}C_6$ carbides are distributed dispersedly along ferrite/ferrite and ferrite/martensite boundaries, and within the ferrite, carbides with smaller size can also be readily seen. For the 9Cr-0.1Al steel, more carbides are precipitated along boundaries with larger size, and carbides are seldom formed in ferrite. Influences of Al addition on carbide distribution can be explained as follows. In mechanical milling, Al element was alloyed with pre-alloyed powders as substitutional solute. Since the presence of Al would decrease the activity coefficient of C in ferrite, i.e. increase the solubility of C in ferrite [29, 30], as the Al addition is increased from 0.05 to 0.1 wt%, precipitation of carbides in ferrite becomes more difficult. Thus, the carbon rejected from ferrite would partition to the grain boundaries, combining with Fe and Cr to produce the $M_{23}C_6$ with larger size.

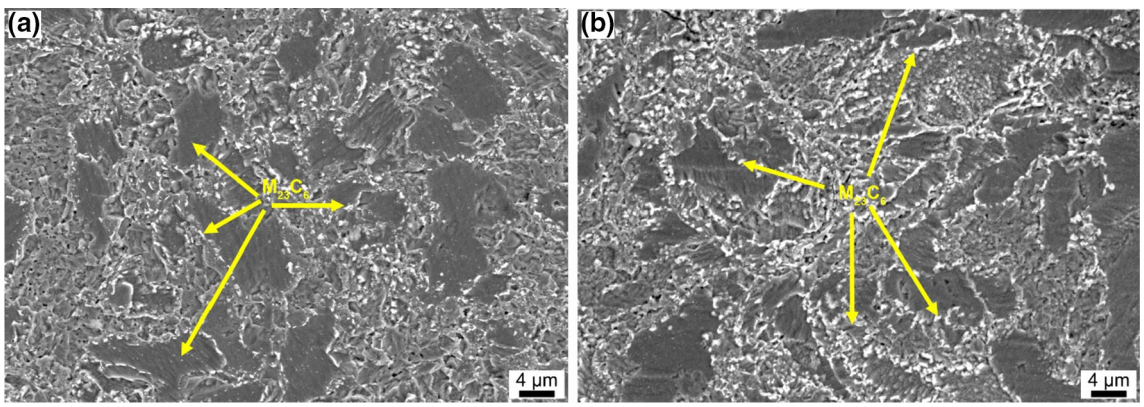

Fig. 5 SEM micrographs of SPSed **a** and **b** 9Cr-0.05Al, and **c** and **d** 9Cr-0.1Al steels

Figure 6a and b respectively shows the oxides in 9Cr-0.05Al and 9Cr-0.1Al steels, and the inset represents the size distribution of oxides. With the Al addition increasing from 0.05 to 0.1 wt%, more oxides with smaller size (< 10 nm) are produced. The average size of oxide nanoparticles in 9Cr-0.05Al and 9Cr-0.1Al steels is respectively determined as 11.1 nm and 9.0 nm. The oxide size is closely related to its type, and it is necessary to identify the oxides in steels. By adding Al, four types of Y–Al–O oxides can be formed, i.e. orthorhombic-$YAlO_3$ (YAP), bcc-$Y_3Al_5O_{12}$ (YAG), momoclinic-$Y_4Al_2O_9$ (YAM), and hexagonal-$YAlO_3$ (YAH) [31]. HRTEM images of oxides in 9Cr-0.05Al and 9Cr-0.1Al steels are shown in Fig. 7. The large isolated oxide nanoparticle (43 nm in diameter) in Fig. 7a is identified to be Y_2O_3 according to the fast Fourier transformation (FFT) image. Small nanoparticles (< 5 nm in diameter) densely distributed are identified to be Y–Al–O complex oxides, $Y_4Al_2O_9$. Notice that the border of large Y_2O_3 contains some $Y_4Al_2O_9$ particles, as indicated by the yellow arrows. This implies that the $Y_4Al_2O_9$ formation is closely related to the Y_2O_3 particle. Figure 7b shows the nanoparticle (about 5 nm in diameter) in 9Cr-0.1Al steel, which is also identified to be YAM particle. Looking into the stoichiometric ratios of four types of Y–Al–O oxides, the $Y_4Al_2O_9$ has the smallest Al/Y ratio. Thus, it is suggested that the favorable formation of $Y_4Al_2O_9$ is associated with the little addition of Al in this work. The oxide formation reaction: $2Y_2O_3 + Al_2O_3 \rightarrow Y_4Al_2O_9$ can take place at temperatures between 900 and 1100 °C [32], which is within the sintering temperature in this work. As the Al addition is increased from 0.05 to 0.1 wt%, the above reaction undergoes more sufficiently, and less large-sized Y_2O_3 particles are remained, which can explain the larger proportion of small oxide nanoparticles (< 10 nm in diameter) in 9Cr-0.1Al steel.

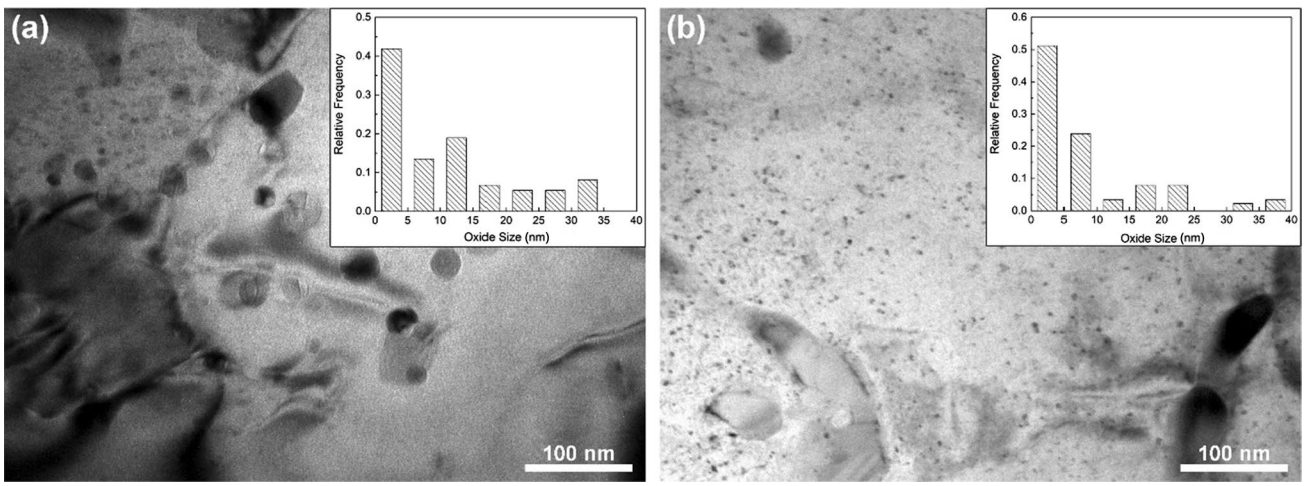

Fig. 6 Oxide nanoparticles in SPSed **a** 9Cr-0.05Al, and **b** 9Cr-0.1Al steels

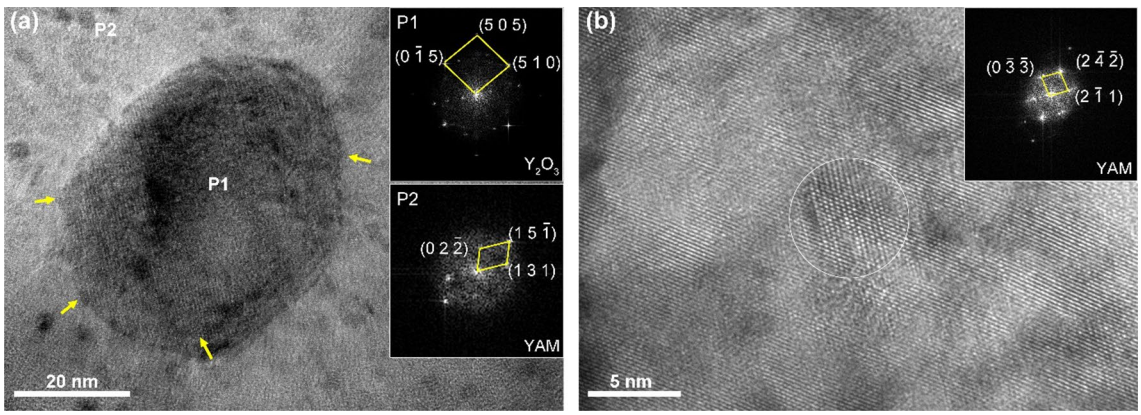

Fig. 7 HRTEM images of oxide nanoparticles in **a** 9Cr-0.05Al and **b** 9Cr-0.1Al steels, as well as the corresponding FFT patterns

3.2 Annealed at 800 °C

For the ferritic/martensitic steels, annealing treatment is mandatory, aimed at restoring ductility and improving microstructure stability at high temperatures. Figure 8a, d respectively shows the optical micrograph of the 9Cr-0.05Al and 9Cr-0.1Al steels subjected to annealing treatment at 800 °C. Figure 8b, e display the distribution of annealed ferrite, respectively. The size distribution of annealed ferrite in 9Cr-0.05Al steel and 9Cr-0.1Al steel is respectively presented in Fig. 8c, f. Compared with the ferrite distribution in sintered condition, the ferrite distributes more uniformly after the annealing treatment. The average ferrite size of 9Cr-0.05Al steel is decreased from 5.1 to 3.2 μm, and that of 9Cr-0.1Al steel is decreased from 5.7 to 3.2 μm. However, the volume fraction (i.e. area fraction) of ferrite in annealed condition is approximately the same as that in sintered condition. In Fig. 4, it can be seen that the dislocation density in ferrite is low. It is not likely to refine the ferrite by the recovery and rearrangement of dislocations and the resultant recrystallization. Actually, if sufficiently large particles are present in the matrix, an additional recrystallization nucleation mechanism can be initiated, namely particle-stimulated nucleation (PSN) of recrystallization. This would promote a more homogeneous and refined grain size distribution [33, 34]. The particle-stimulated nucleation of recrystallization depends on particle size and strain. In aluminum, iron, copper and nickel, PSN was found to occur at particles of diameter greater than approximately 1 μm, while a lower limit of 0.8 μm was inferred from the indirect measurements on Fe–C alloys [33]. Upon annealing, $M_{23}C_6$ carbides will precipitate from tempered martensite, and the $M_{23}C_6$ in sintered condition will grow further. Figure 9 shows the SEM micrographs of the annealed 9Cr-0.05Al and 9Cr-0.1Al steels, as well as the size distribution of $M_{23}C_6$ carbides. In both steels, the $M_{23}C_6$ carbides in tempered martensite are much smaller than those along ferrite/ferrite and ferrite/tempered martensite boundaries, while the density of carbides in tempered martensite is larger, as shown in Fig. 9a, b, d, e. In 9Cr-0.1Al steel, the $M_{23}C_6$ along ferrite/ferrite and ferrite/tempered martensite boundaries are still larger than those in 9Cr-0.05Al steel. From the insets in Fig. 9c, f, it can be seen certain amount of $M_{23}C_6$ with size larger than 0.8 μm exist, which is related to the coarsening of $M_{23}C_6$ along boundaries in annealing. These coarse $M_{23}C_6$ may initiate particle-stimulated nucleation of recrystallization, leading to the homogeneous and refined distribution of ferrite.

Figures 10 and 11 respectively displays the microstructural characteristics of annealed 9Cr-0.05Al and 9Cr-0.1Al steels. As indicated by the dotted line in Fig. 10a, one large sized ferrite grain can be distinguished. It is noted that at the boarder of the large sized ferrite, two equiaxed ferrite grains with smaller size are formed, and one ferrite is adjacent to the large sized $M_{23}C_6$ up to about 550 nm. Combing with the particle-stimulated nucleation of recrystallization, the two small ferrite grains formed within the original large sized ferrite are suggested to be recrystallized ferrite. Annealed martensite surrounded by ferrite grains is

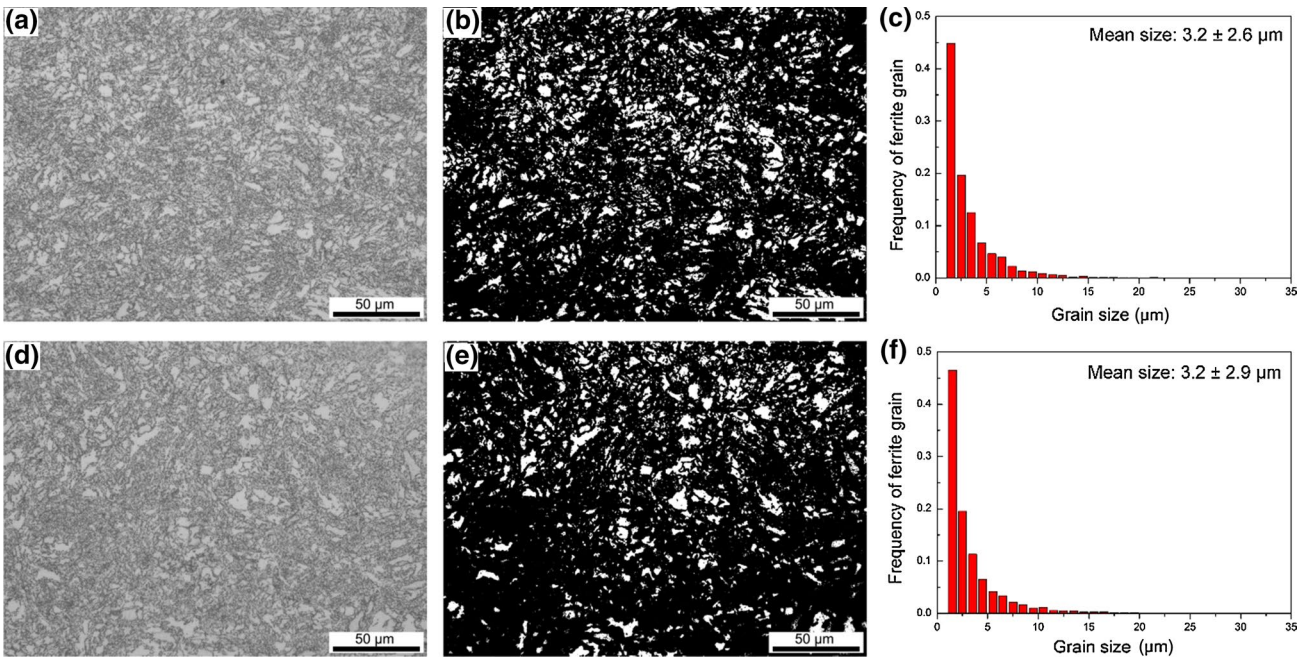

Fig. 8 Optical micrograph, ferrite distribution and the size frequency of ferrite in annealed 9Cr-ODS steels with different Al contents. **a**–**c** 0.05 wt% Al added, and **d**–**f** 0.1 wt% Al added

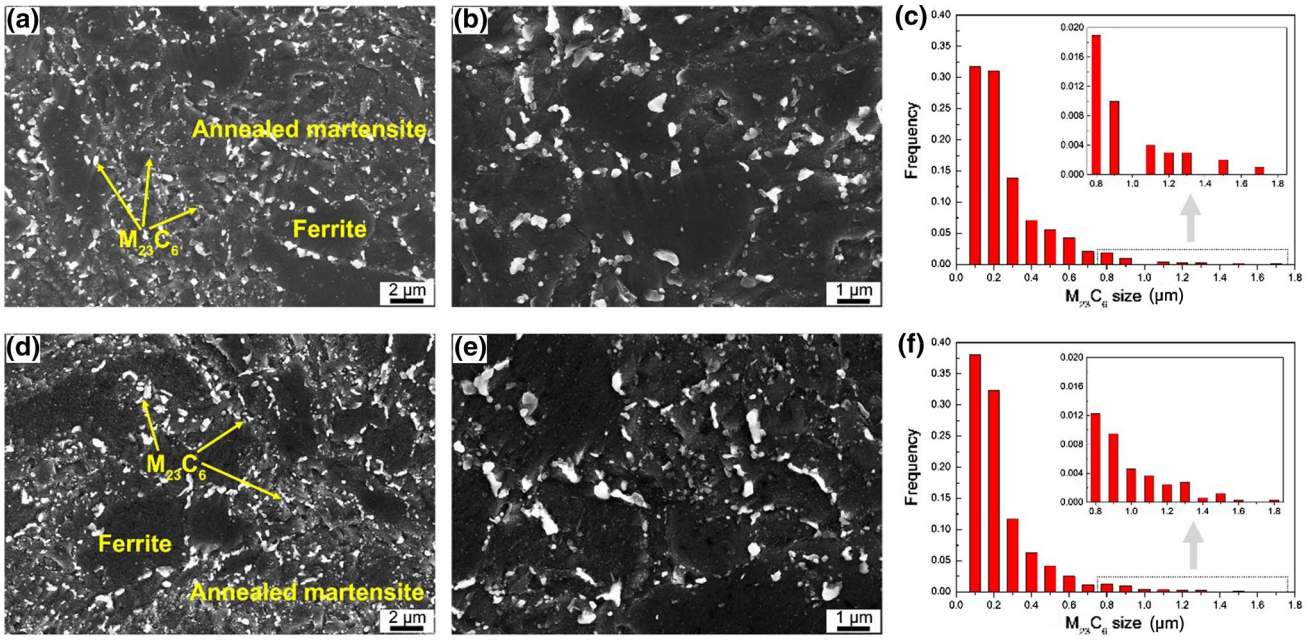

Fig. 9 SEM micrographs under different magnification times and the size frequency of $M_{23}C_6$ in annealed 9Cr-ODS steels with different Al contents. **a**–**c** 0.05 wt% Al added, and **d**–**f** 0.1 wt% Al added

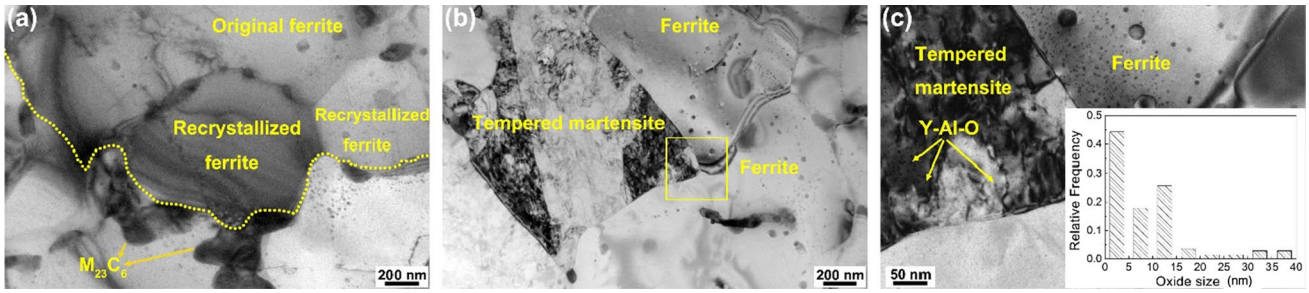

Fig. 10 TEM images showing the **a** recrystallized ferrite, **b** annealed martensite and **c** the annealed ferrite/martensite interphase boundary in annealed 9Cr-0.05Al steel

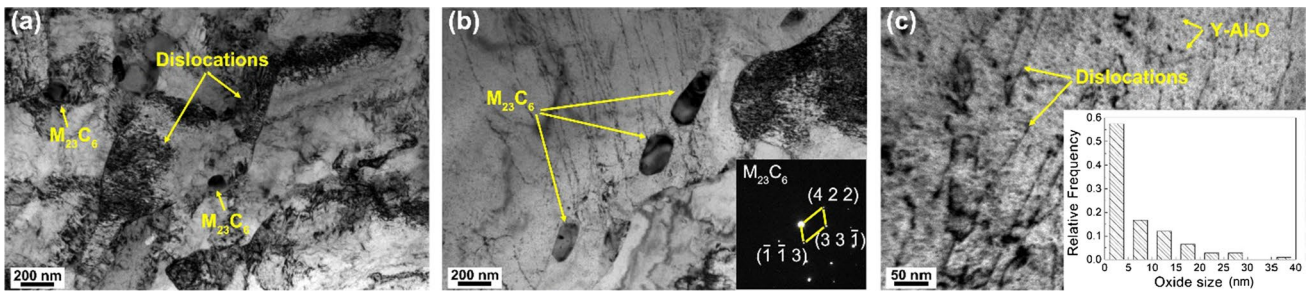

Fig. 11 TEM images showing the **a** annealed martensite with high density of dislocations, **b** carbides in ferrite and **c** the dislocations and oxides in annealed 9Cr-0.05Al steel

shown in Fig. 10b. High density of dislocations can still be observed in annealed martensite, despite of the dislocation recovery in annealing, and no recrystallized grains are found. Figure 10c shows the rectangle part in Fig. 10b with higher magnification times. Large amount of Y–Al–O oxide nanoparticles can be clearly seen in annealed martensite. These

fine sized nanoparticles would effectively pin the dislocation motion, retarding the dislocation recovery in annealing. For the annealed 9Cr-0.1Al steel, it seems that the dislocation density in annealed martensite is higher than that in the 9Cr-0.05Al steel (Fig. 11a), which can be explained by the more Y–Al–O particles smaller than 10 nm in 9Cr-0.1Al steel. Dislocations are tangled together in annealed martensite, and small sized $M_{23}C_6$ (about 100 nm) are precipitated at lath boundaries. $M_{23}C_6$ carbides with larger size (> 200 nm) are found near the ferrite boundaries, as shown in Fig. 11b. The growth of $M_{23}C_6$ within ferrite is related to Ostwald ripening. In the annealed ferrite, the dislocations are also pinned by the densely distributed Y–Al–O oxides. Insets in Figs. 10c and 11c represent the size distribution of oxides in annealed steels. The average size of oxide nanoparticles in 9Cr-0.05Al and 9Cr-0.1Al steels is respectively determined as 9.0 and 7.7 nm, smaller than those in sintered condition. Due to the fast heating rate and short holding time in SPS consolidation, the Y–Al–O cannot be fully precipitated in sintering. Annealing treatment would promote the precipitation of fine Y–Al–O oxides. Thus, the average size of oxide nanoparticles in annealed steel is decreased.

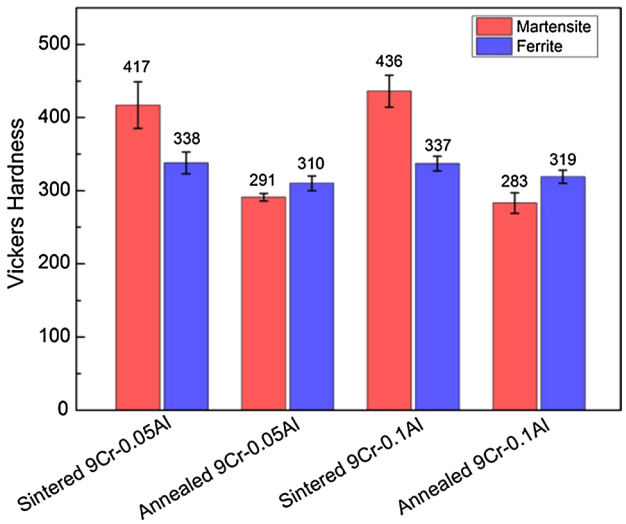

Fig. 12 Hardness of martensite and ferrite in 9Cr-0.05Al and 9Cr-0.1Al steels under sintered and annealed conditions

3.3 Hardness Behavior

Hardness of a material characterizes the resistance of the material against plastic deformation [27]. Figure 12 shows the hardness of martensite and ferrite in both sintered and annealed 9Cr-0.05Al and 9Cr-0.1Al steels. It can be seen despite of Al addition, there is little difference in hardness of martensite or ferrite in 9Cr-0.05Al and 9Cr-0.1Al steels. In sintered condition, the hardness of martensite is higher than that of ferrite. However, after the annealing treatment, the hardness of martensite drops sharply, while the hardness of ferrite changes slightly. The decrease in hardness of martensite after annealing treatment can be ascribed to the dislocation recovery. It is interesting to note that in annealed condition, the hardness of ferrite is higher than that of martensite. The dislocation density in annealed martensite is larger than that in annealed ferrite. The higher hardness of annealed ferrite compared to annealed martensite may be related to oxide nanoparticles. One possible mechanism is that Al as a ferrite stabilizer may partition into ferrite upon austenite to ferrite transformation, facilitating the formation of Y–Al–O oxides, which in turn increases the hardness of annealed ferrite.

3.4 Tensile Strength and Fractograph

Tensile flow curves and fracture surfaces of the sintered 9Cr-Al ODS steels tested at room temperature are shown in Fig. 13. The ultimate tensile strengths of the sintered 9Cr-0.05Al and 9Cr-0.1Al steels are respectively determined to be 1172 ± 12 MPa and 1200 ± 9 MPa. As the Al addition increases, the tensile strength of sintered 9Cr-Al ODS steel is slightly increased, which is related to the formation of fine

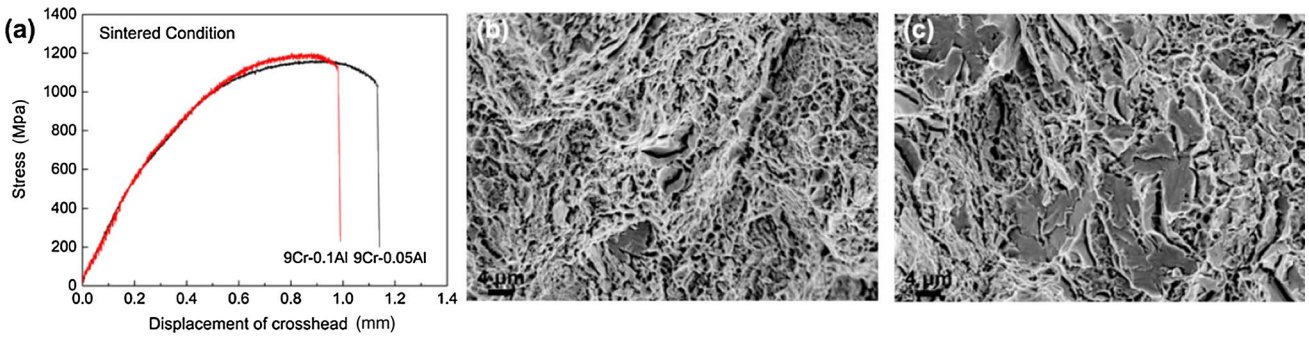

Fig. 13 **a** Tensile flow curves of the sintered 9Cr-Al ODS steels tested at room temperature and tensile fracture surfaces of the sintered, **b** 9Cr-0.05Al and **c** 9Cr-0.1Al steels

Y–Al–O oxide nanoparticles. The total elongation of the sintered 9Cr-0.05Al steel is larger than that of 9Cr-0.1Al steel. In Fig. 13b, c, the amount of dimples of the 9Cr-0.05Al steel is larger than that of 9Cr-0.1Al steel, and transgranular fracture of the ferrite can be seen on the fracture surface of the sintered 9Cr-0.1Al steel. Although the volume fraction of ferrite in 9Cr-0.05Al steel is larger than 9Cr-0.1Al steel, more large-sized ferrite grains are present in the 9Cr-0.1Al steel, as shown in Figs. 1c, f. In tensile loading, as the dislocations cross over the nanoparticles, dislocations will be piled up at grain boundaries, and these large-sized ferrites would facilitate the stress concentration, resulting in the prefailure of the 9Cr-Al steel.

Since the transformable 9Cr-ODS steels are always served in annealed condition, the tensile performance of annealed 9Cr-Al steels is more concerned, and the result is shown in Fig. 14a. The ultimate tensile strengths of the annealed 9Cr-0.05Al and 9Cr-0.1Al steels are respectively determined to be 980 ± 10 and 940 ± 12 MPa. With the Al addition increasing, the ultimate tensile strength of annealed 9Cr-Al steel is decreased. Both steels exhibit poor ductility, and the ductility of the annealed 9Cr-0.1Al steel is worse. Compared with the 9Cr-ODS steel without Al addition [28], although Al addition contributes to the decrease in average size of oxide nanoparticles, the mechanical performance of the 9Cr-ODS steel is not improved significantly. Moreover, Al addition quite impedes the ductility. To reveal the factors accounting for the decreased tensile strength and ductility of annealed 9Cr-0.1Al steel, fracture surfaces of these two steels are examined, as shown in Fig. 14b, c. Fracture behaviors of annealed 9Cr-0.05Al and 9Cr-0.1Al steels are quite different. With respect to the annealed 9Cr-0.05Al steel, dimple fracture is dominated, and on certain part of the fracture surface, smooth fracture surface of annealed ferrite can be observed. As for the annealed 9Cr-0.1Al steel, the fracture surface is characterized by the dimple fracture and intergranular fracture of annealed ferrite. By the comparison between Fig. 14b, c, the following differences can be identified: (1) the dimple size of annealed 9Cr-0.05Al steel is larger than that of annealed 9Cr-0.1Al steel; (2) the fracture surface of ferrite in annealed 9Cr-0.05Al steel is much flatter, and on it slip band can be observed; nevertheless, the fracture surface of ferrite in annealed 9Cr-0.1Al steel is irregular and uneven, and no slip bands are observed; (3) $M_{23}C_6$ carbides are exposed on the fracture surface of ferrite in annealed 9Cr-0.1Al steel. The smaller dimple size of annealed 9Cr-0.1Al steel is related to the fine distribution of oxides in it. The different fracture behaviors of annealed ferrites are suggested to be the primary factors affecting the tensile performances of annealed 9Cr-0.05Al and 9Cr-0.1Al steels. Annealed ferrite has a higher hardness than annealed martensite. In tensile loading, the dislocation would concentrate at annealed ferrite/martensite boundaries, stimulating stress concentration. On the other hand, with the Al content increasing, larger sized $M_{23}C_6$ carbides tend to form at or adjacent ferrite/martensite boundaries and ferrite/ferrite boundaries. These $M_{23}C_6$ would further deteriorate the boundary strength, facilitating cracking growth. Thus, the fracture of ferrite in annealed 9Cr-0.1Al steel exhibits intergranular fracture characteristics.

4 Conclusions

Dual-phase transformable Al-alloyed 9Cr-ODS steels can be fabricated by spark plasma sintering, with martensite and transformed ferrite as phase constituents. It is found that Al content has an evident effect on the amount of the transformed ferrite, distribution and sizes of $M_{23}C_6$ particles in the ferrite, and the formation of fine Y–Al–O oxide nanoparticles. Upon annealing treatment at 800 °C, the coarse $M_{23}C_6$ will stimulate recrystallization nucleation of the ferrite, resulting in the homogeneous distribution and refinement of ferrite grains. As Al addition increases, the tensile strength of the sintered 9Cr-Al steel will be increased, while the tensile strength of the annealed 9Cr-Al steel will be decreased. Both large-sized ferrite grains and coarse $M_{23}C_6$ carbides will deteriorate the ductility of the 9Cr-Al ODS steels.

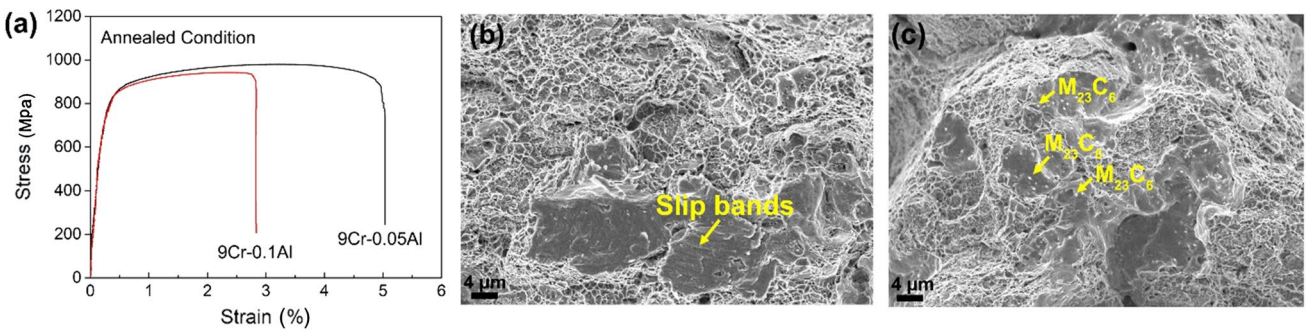

Fig. 14 **a** Stress–strain curves of the annealed 9Cr-Al ODS steels tested at room temperature and tensile fracture surfaces of the annealed, **b** 9Cr-0.05Al and **c** 9Cr-0.1Al steels

Acknowledgements The authors are grateful to the China National Funds for Distinguished Young Scientists (Granted No. 51325401), the National Natural Science Foundation of China (Granted Nos. 51474156 and U1660201), the National Magnetic Confinement Fusion Energy Research Program (Granted No. 2014GB125006) for grant and financial support.

References

1. T.K. Kim, S. Noh, S.H. Kang, J.J. Park, H.J. Jin, M.K. Lee, J. Jang, C.K. Rhee, Nucl. Eng. Technol. **48**, 572–594 (2016)
2. S. Ukai, M. Fujiwara, J. Nucl. Mater. **307**, 749–757 (2002)
3. X. Zhou, C. Liu, L. Yu, Y. Liu, H. Li, J. Mater. Sci. Technol. **31**, 235–242 (2015)
4. Y. Zhou, Y. Liu, X. Zhou, C. Liu, J. Yu, Y. Huang, H. Li, W. Li, J. Mater. Sci. Technol. **33**, 1448–1456 (2017)
5. I.S. Kim, B.Y. Choi, Met. Mater. Int. **8**, 265–270 (2002)
6. C. Capdevila, I. Toda-Caraballo, G. Pimentel, J. Chao, Met. Mater. Int. **18**, 799–804 (2012)
7. G.R. Odette, M.J. Alinger, B.D. Wirth, Annu. Rev. Mater. Res. **38**, 471–503 (2008)
8. H. Xu, Z. Lu, S. Ukai, N. Oono, C. Liu, J. Alloys Compd. **693**, 177–187 (2017)
9. T. Yamashiro, S. Ukai, N. Oono, S. Ohtsuka, T. Kaito, J. Nucl. Mater. **472**, 247–251 (2016)
10. M.S. El-Genk, J.-M. Tournier, J. Nucl. Mater. **340**, 93–112 (2005)
11. S. Ukai, S. Ohtsuka, Energy Mater. **2**, 26–35 (2007)
12. T. Tanno, S. Ohtsuka, Y. Yano, T. Kaito, Y. Oba, M. Ohnuma, S. Koyama, K. Tanaka, J. Nucl. Mater. **440**, 568–574 (2013)
13. S. Ohtsuka, T. Kaito, T. Tanno, Y. Yano, S. Koyama, K. Tanaka, J. Nucl. Mater. **442**, S89–S94 (2013)
14. S. Ukai, S. Ohtsuka, T. Kaito, H. Sakasegawa, N. Chikata, S. Hayashi, S. Ohnuki, Mater. Sci. Eng., A **510**, 115–120 (2009)
15. M. Yamamoto, S. Ukai, S. Hayashi, T. Kaito, S. Ohtsuka, Mater. Sci. Eng., A **527**, 4418–4423 (2010)
16. R. Miyata, S. Ukai, X. Wu, N. Oono, S. Hayashi, S. Ohtsuka, T. Kaito, J. Nucl. Mater. **442**, S138–S141 (2013)
17. S. Ohtsuka, S. Ukai, M. Fujiwara, J. Nucl. Mater. **351**, 241–246 (2006)
18. S. Ohtsuka, S. Ukai, H. Sakasegawa, M. Fujiwara, T. Kaito, T. Narita, J. Nucl. Mater. **367**, 160–165 (2007)
19. H. Xu, Z. Lu, S. Ukai, N. Oono, C. Liu, J. Alloys Compd. **693**, 177–187 (2017)
20. G. Zhang, Z. Zhou, K. Mo, Y. Miao, S. Li, X. Liu, M. Wang, J.-S. Park, J. Almer, J.F. Stubbins, Mater. Design **98**, 61–67 (2016)
21. K.A. Unocic, B.A. Pint, D.T. Hoelzer, J. Mater. Sci. **51**, 9190–9206 (2016)
22. A.J. London, S. Santra, S. Amirthapandian, B.K. Panigrahi, R.M. Sarguna, S. Balaji, R. Vijay, C.S. Sundar, S. Lozano-Perez, C.R.M. Grovenor, Acta Mater. **97**, 223–233 (2015)
23. H. Xu, Z. Lu, D. Wang, C. Liu, Nucl. Eng. Technol. **49**, 178–188 (2017)
24. P. Dou, A. Kimura, R. Kasada, T. Okuda, M. Inoue, S. Ukai, S. Ohnuki, T. Fujisawa, F. Abe, J. Nucl. Mater. **442**, S95–S100 (2013)
25. S. Ohtsuka, T. Kaito, M. Inoue, T. Asayama, S.W. Kim, S. Ukai, T. Narita, H. Sakasegawa, J. Nucl. Mater. **386**, 479–482 (2009)
26. H. Oka, T. Tanno, S. Ohtsuka, Y. Yano, T. Uwaba, T. Kaito, M. Ohnuma, Nucl. Mater. Energy **9**, 346–352 (2016)
27. E. Mittemeijer, *Fundamentals of materials science: the microstructure–property relationship using metals as model systems* (Springer, Heidelberg, 2010)
28. X. Zhou, Y. Liu, L. Yu, Z. Ma, Q. Guo, Y. Huang, H. Li, Mater. Des. **132**, 158–169 (2017)
29. W.C. Leslie, G.C. Rauch, Metall. Mater. Trans. A **9**, 343–349 (1978)
30. H. Xue, T.N. Baker, Mater. Sci. Technol. **9**, 424–429 (1993)
31. G. Zhang, Z. Zhou, K. Mo, P. Wang, Y. Miao, S. Li, M. Wang, X. Liu, M. Gong, J. Almer, J.F. Stubbins, J. Alloys Compd. **648**, 223–228 (2015)
32. L. Wen, X. Sun, Z. Xiu, S. Chen, C.-T. Tsai, J. Eur. Ceram. Soc. **24**, 2681–2688 (2004)
33. F.J. Humphreys, M. Hatherly, *Recrystallization and related annealing phenomena* (Elsevier, Oxford, 2004)
34. J. Konrad, S. Zaefferer, D. Raabe, Acta Mater. **54**, 1369–1380 (2006)